OPEN ACCESS

Transient Simulation of Diffusion-Limited Electrodeposition Using Volume of Fluid (VOF) Method

To cite this article: E. Karimi-Sibaki *et al* 2023 *J. Electrochem. Soc.* **170** 072501

View the article online for updates and enhancements.

Transient Simulation of Diffusion-Limited Electrodeposition Using Volume of Fluid (VOF) Method

E. Karimi-Sibaki,[1] A. Vakhrushev,[1] M. Wu,[2] A. Ludwig,[2] J. Bohacek,[3] and A. Kharicha[1,z]

[1]*Christian-Doppler Laboratory for Metallurgical Applications of Magnetohydrodynamics, Montanuniversitaet of Leoben, A-8700 Leoben, Austria*
[2]*Chair of Simulation and Modeling of Metallurgical Processes, Montanuniversitaet of Leoben, A-8700 Leoben, Austria*
[3]*Heat Transfer and Fluid Flow Laboratory, Faculty of Mechanical Engineering, Brno University of Technology, Technicka 2896/2, 616 69 Brno, Czech Republic*

A numerical model utilizing the volume of fluid (VOF) method is proposed to simulate the transient shape changes of the deposit front, considering the diffusion-limited electrodeposition process. Modeling equations are proposed to accurately handle transport phenomena in both electrolyte (fluid) and deposit (solid). Transient evolutions of field structures, including flow, concentration, electric current density, and electric potential, are computed considering electrodeposited copper bumps. Two cases, including single cavity and multiple cavities, are studied. Based on the modeling results, the maximum height of the hump and the thickness of the deposited layer in each consecutive cavity decreases going from upstream to downstream. Conversely, the location of the maximum height of the hump remains unchanged in all cavities. Results are validated against available experiments.

Supplementary material for this article is available online

List of Symbols

a	Cell size	m
a_{VOF}	Interface area	m^2
c	Concentration of cupric ion	mol m^{-3}
c_∞	Bulk concentration of cupric ion	mol m^{-3}
$D_{Cu^{2+}}$	Diffusion coefficient of cupric ion	m^2 s^{-1}
F	Faraday constant	A s mol^{-1}
g	Gravity constant	m s^{-2}
h_1	Photoresist film thickness	m
h_2	Flow inlet/outlet thickness	m
h_{Pe}	Characteristic length of Pe number	m
$\vec{j}$	Electric current density	A m^{-2}
L_1	Length of electrode	m
L_2	Length of outlet region	m
L_3	Length of inlet region	m
$\dot{m}$	Mass source	kg m^{-3} s^{-1}
M	Molecular weight	g mol^{-1}
$\vec{n}(n_x, n_y)$	Unit normal vector	
p	Pressure	Pa
R	universal gas constant	J K^{-1} mol^{-1}
S_u	Momentum sink term	N m^{-3} s^{-1}
S_φ	Electric potential sink term	A m^{-3} s^{-1}
S_c	Concentration sink term	mol m^{-3} s^{-1}
Sh	Sherwood number	
t	Time	s
$\vec{u}$	Velocity vector	m s^{-1}
u_∞	Bulk velocity	m s^{-1}
u_{df}	Deposit front velocity	m s^{-1}
V	Volume of the computational cell	m^3
V_{app}	Applied voltage	V
V_d	Deposit volume in the computational cell	m^3
$\vec{x}$	Vector coordinates	m
x, y	Coordinates	m

(Continued).

X, Y	Dimensionless coordinates	
$z_{Cu^{2+}}$	Charge number of cupric ion	
β	Volume fraction of deposit	
β_L	Limit volume fraction of deposit	
ρ	Density	kg m^{-3}
ρ_d	Deposit density	kg m^{-3}
ρ_e	Electrolyte density	kg m^{-3}
μ	Dynamic viscosity	kg s^{-1} m^{-1}
μ_d	Deposit viscosity	kg s^{-1} m^{-1}
μ_e	Electrolyte viscosity	kg s^{-1} m^{-1}
φ	Electric potential	V
σ	Electrical conductivity	S m^{-1}
σ_e	Electrical conductivity of electrolyte	S m^{-1}
σ_d	Electrical conductivity of deposit	S m^{-1}
()*	A normalized parameter	

The electrodeposition process, composed of cathode/anode electrodes and the electrolyte, is extensively used for the synthesis of micro-electromechanical systems (MEMS)[1,2] The metal (e.g. iron, gold, silver, copper, zinc, nickel, etc.) present in the electrolyte solution is reduced through faradaic reactions to form a metal layer at the electrode surface.[3] The metal layer grows during the process, whereby the metal deposit front continuously deforms because of both electrochemical mass transfer at the metal-electrolyte interface and the presence of electromagnetic and viscous forces. Conventionally, the thickness of the metal layer and the shape (profile) of the deposit front are criteria to assess the performance of the process[3] Therefore, understanding the transient growth of the metal layer, e.g. through numerical simulations, is a crucial step towards optimizing the electrodeposition process.

From a modeling point of view, electrodeposition is a multi-physics problem involving mass transfer, heat transfer, fluid flow, and magnetohydrodynamics (MHD). A wide range of methods has been proposed to simulate the electrodeposition process. Early studies suggested the use of the finite element method (FEM)[4,5] or finite difference method (FDM)[6–8] to handle governing equations related to electrodeposition. Also, Chalupa et al.[9] used the explicit finite volume method (FVM) and the boundary element method

zE-mail: abdellah.kharicha@unileoben.ac.at
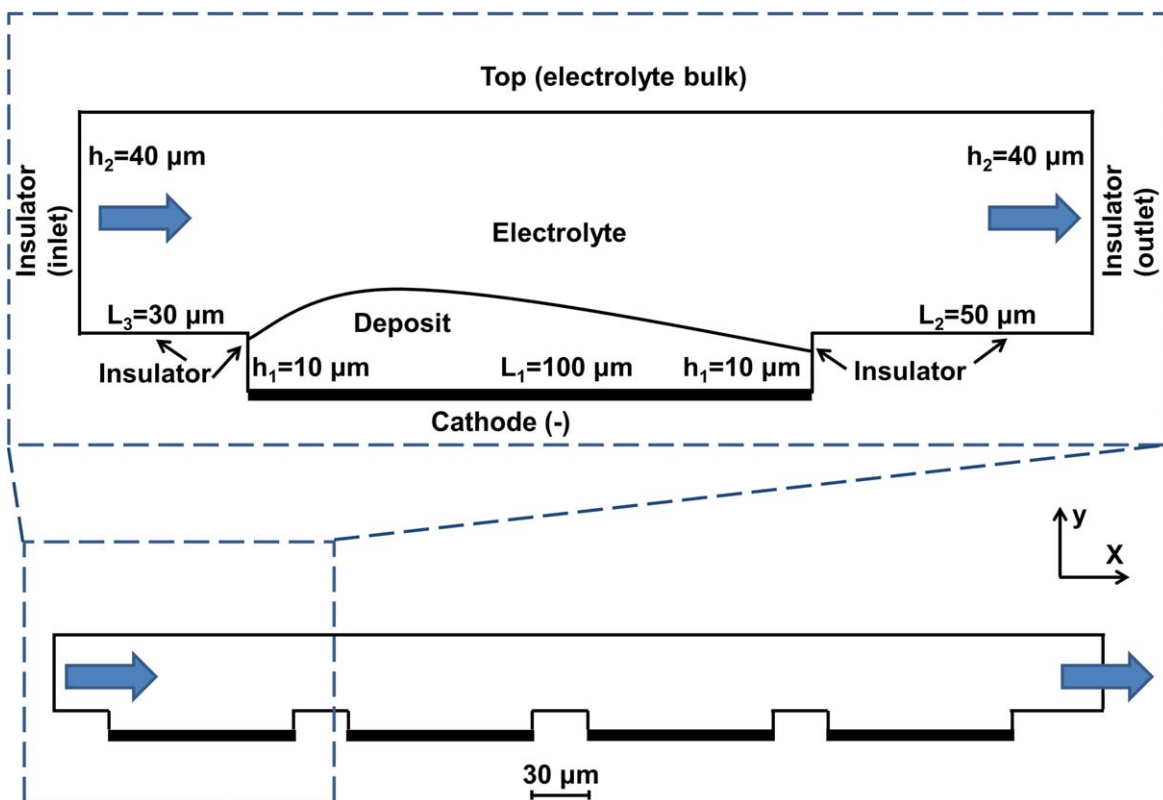
Figure 1. Schematic illustration of the computational domain and boundaries for case studies, including single and multiple cavities.

(BEM) to simulate electrodeposition in a submicron trench. They pointed out that BEM has the advantage of high computational speed and high solution stability compared to explicit FVM. However, BEM is unsuitable for simulating transient diffusion effects on a continuously deforming domain.[9] Schanz[10] also gave a similar conclusion that BEM is inadequate for all types of non-linear problems.

More recently, Monte Carlo,[11] phase-field,[12–14] level set,[6,15] and dynamic mesh[16,17] techniques were proposed to simulate the transient electrodeposition process. For the application of Monte Carlo or phase-field methods, which have an enormous computational cost, thermodynamic data of free energy or entropy are required. A transition zone to specify a smooth function is needed around the (diffuse) interface using the Level set method. The transition zone covers multiple cells spanning the exact interface location. Reinitialization of the function at each time step is essential as the shape of the function must remain the same as the interface.[6,15] Dynamic mesh is advised for problems involving unidirectional deformation of boundaries.[16,17]

Focusing on the simulation of electrodeposition in trenches or cavities with application to microelectronics, the finite difference method (FDM)[6,18] or finite element method (FEM)[19,20] were utilized to discretize governing equations. Indeed, the popular COMSOL Multiphysics software offers a package based on the FEM method to simulate the electrodeposition process. For instance, Gu et al.[21] used COMSOL to study electrodeposited nickel bumps. They evaluated the influence of current density and microvia geometries on the shape evolution of the deposited layer, intending to obtain finer solder bumps for chip-scale packaging (CSP).

Previously, we proposed a volume of fluid (VOF) based model to study the electrodeposition process considering the secondary current distribution.[22] The discretization scheme is according to the finite volume method (FVM), which automatically conserves mass, momentum and species concentration.[23] VOF based model creates a sharp interface that occupies only one computational cell as

the thickness of the interface. Also, VOF based model allows us to capture any deposit front profile, regardless of process size and geometric configuration. Here, we extend the model to include the influence of the ion concentration field on the transient shape change of the deposition front. The model is examined considering the electrodeposition of copper bumps, as schematically shown in Fig. 1. Electrochemical systems involving a single cavity and multiple cavities are investigated. The proposed VOF based model provides insight into the transport of ions to the constantly deforming depositional front under conditions of forced convection.

Modeling

All symbols are described in "List of Symbols". The electrolyte (liquid phase) and the metal deposit (solid phase) are considered two immiscible and incompressible phases. All governing equations are listed in Table I.

According to the volume of fluid (VOF) method[24] the two phases are recognized considering a spatial and temporal-dependent marker function (β) as described in Eq. 1. An advection equation is solved for β on a fixed Eulerian grid to model the transport of interface as described in Eq. 2. The local growth of cathode surface is taken into account as a mass source term in the advection equation for β as described in Eq. 3. The mass source term is calculated considering the unit normal vector ($\vec{n}$) at the interface and the interface area (a_{VOF}) in each computational cell.[8,22] Of note, the mass source is only applied at the computational cells of the interface, where ($0 < \beta < 1$). After completion of deposition ($\beta = 1$) in a cell, the interface shifts to the adjacent cell, which is identified using the unit normal vector ($\vec{n}$) indicating the growth direction. The unit normal vector ($\vec{n}$) is calculated through Eq. 4.

The limit volume fraction (β_L) is calculated through Eq. 5, which enables us to determine the exact interface area[22] at each computational cell, exploiting Eq. 6. Of note, the proposed equations to calculate interface area are only valid for quadrilateral square shaped

Table I. Governing equations of volume fraction, flow, concentration of reactant, and electric current density fields.

Volume fraction

$$\beta(\vec{x}, t) = \frac{V_d}{V} = \begin{cases} 1, & \vec{x} \in \text{Deposit} \\ 0 < \beta < 1, & \vec{x} \in \text{Interface} \\ 0, & \vec{x} \in \text{Electrolyte} \end{cases} \quad (1)$$

$$\frac{\partial \beta}{\partial t} + \nabla \cdot (\beta u) = \frac{\dot{m}}{\rho_d} \quad (2)$$

$$\dot{m} = \frac{a_{\text{VOF}} M}{zFV}(\vec{j} \cdot \vec{n}) \quad (3)$$

$$\vec{n} = (n_x, n_y) = \frac{\vec{\nabla} \beta}{\|\vec{\nabla} \beta\|} \quad (4)$$

$$\beta_L = \min\left(\frac{|n_y|}{2|n_x|}, \frac{|n_x|}{2|n_y|}\right) \quad (5)$$

$$a_{\text{VOF}} = \begin{cases} \sqrt{\dfrac{2\beta a^2}{|n_x||n_y|}}, & 0 < \beta < \beta_L \\[2mm] \min\left(\dfrac{a}{|n_x|}, \dfrac{a}{|n_y|}\right), & \beta_L < \beta < 1 - \beta_L \\[2mm] \sqrt{\dfrac{2(1-\beta)a^2}{|n_x||n_y|}}, & \beta_L < \beta < 1 \end{cases} \quad (6)$$

Flow field

$$\nabla \cdot u = \dot{m}\left(\frac{1}{\rho_d} - \frac{1}{\rho_e}\right) \quad (7)$$

$$\frac{\partial \rho u}{\partial t} + \nabla \cdot (\rho u u) = -\nabla p + \nabla \cdot [\mu(\nabla u + \nabla u^T)] \\ + \rho g - \frac{\mu}{K}\beta u \quad (8)$$

Concentration field of Cu^{2+}

$$\frac{\partial c}{\partial t} = -\nabla \cdot [\vec{u} c - D_{Cu^{2+}} \nabla c] - \frac{\beta}{K}c \quad (9)$$

Electric current density

$$\nabla \cdot (-\sigma \nabla \varphi) = -\frac{\beta}{K}\varphi \quad (10)$$

$$\vec{j} = -\sigma \nabla \varphi \quad (11)$$

mesh elements. A detailed derivation of Eq. 5 and Eq. 6 is discussed in Ref. 22.

The flow field is determined through continuity, Eq. 7, and momentum, Eq. 8, conservation. The density, $\rho = \beta \rho_d + (1 - \beta)\rho_e$, and the viscosity, $\mu = \beta \mu_d + (1 - \beta)\mu_e$, are the weighted average of phases in each computational cell. Originally, the VOF method was proposed to simulate multiphase systems involving gas-liquid and liquid-liquid[24] Herein, special care must be taken to model the solid deposit utilizing sink terms. For that purpose, the sink term for momentum $\left(S_u = -\frac{\mu}{K}\beta u\right)$, the sink term $\left(S_c = -\frac{\beta}{K}c\right)$ for concentration, Eq. 9, and the sink term $\left(S_\varphi = -\frac{\beta}{K}\varphi\right)$ for electric potential, Eq. 10, are specified. Using a very small value for permeability (e.g. $K = 10^{-10}$) effectively yields zero velocity, zero potential and zero concentration of the reactant within the deposit.[22]

The flow must be ceased within the deposit and at the interface considering the no-slip condition. The deposit front only shifts due to converting ions in the electrolyte to atoms at the interface. Thus, the momentum sink is applied at the computational cells occupied by the interface and the deposit ($\beta > 0$).

The migration flux of the electro-active ion is ignored in the presence of supporting electrolyte.[25] Thus, the concentration field for the cupric ion (Cu^{2+}) is determined by solving the non-steady

diffusion-advection through Eq. 9. The concentration sink term $\left(S_c = -\frac{\beta}{K}c\right)$ acts at computational cells fully occupied by the deposit ($\beta = 1$). Under diffusion-limited condition,[25] the current density at the deposit front is computed as follows: $\vec{j} \cdot \vec{n} = Fz_{Cu^{2+}}D_{Cu^{2+}}\frac{\partial c}{\partial n}$. Considering Eq. 3 and the diffusion-limited condition, the current density solely depends on the gradient of concentration of the reactant at the deposit front. Thus, computation of the time-varying concentration field is sufficient to capture the transient shape change during electrodeposition. In other words, calculating electric current density in the whole system is unnecessary. On the other hand, the computed field structures involving electric current density and electric potential enable engineers to get insight into transport phenomena and to improve the design of the process.

Thus, we also solved the Laplace equation, Eq. 10, to obtain the electrolyte potential field. The electrical conductivity of metal is several orders of magnitudes larger than that of the electrolyte. Therefore, to model the minimal electric field within the deposit, the sink term for electric potential $\left(S_\varphi = -\frac{\beta}{K}\varphi\right)$ is applied at computational cells fully occupied by the deposit ($\beta = 1$). The electric current density is calculated using Ohm's law through Eq. 11.

All transport phenomena, including flow, concentration, and electric potential, are calculated using the well-established Finite Volume Method (FVM) to discretize the governing equations.[23] The temporal discretization scheme is first-order implicit, whereas the spatial scheme is third-order MUSCL.[23] The explicit scheme to discretize volume fraction, Eq. 2, is based on Geo-Reconstruct.[26]

Several User-defined functions (UDF) are implemented in the commercial CFD software, ANSYS FLUENT v.17.1, to accurately model electrodeposition.[27] The models were configured based on the study conducted by Kondo et al.[28,29] The computational domain and boundaries are schematically illustrated in Fig. 1.

Computational domains were filled using quadrilateral square-shaped mesh elements. To ensure that the simulation results are invariant as the mesh is refined, we performed a grid independence study considering two different mesh element sizes, including 1 and 0.5 μm. Our simulation trials revealed that the calculated deposition front profile is independent of the grid size. Of note, the computational domain corresponding to the single cavity contains 32800 structured elements with a size of 0.5 μm. Also, the computational domain involving multiple cavities is filled with 107200 cell elements. An inlet and outlet enclose the systems.

Following Kondo et al.,[28,29] a linear profile of the velocity is assigned at the inlet. All boundary conditions of flow, the concentration of the reactant, and electric potential fields are thoroughly described in Table II.

All parameters used in calculations are listed in Table III. Of note, during our transient computation, the Courant (CFL) number, $\frac{\Delta t}{a}\max(u, u_{df})$, where $u_{df} = \left(\frac{M}{zF\rho}\vec{j} \cdot \vec{n}\right)$ must be kept much smaller than one to attain a converged solution.

Applying the proposed method to investigate large systems involving an enormous number of mesh elements necessitates the use of parallel computation. However, the parallel implementation of the algorithm must be carefully optimized in order to ensure a cost-effective computation time. Herein, the computation time on a single processor Intel Core i7–4790 K CPU 4.00 GHz is about half an hour (single cavity) or a few hours (multiple cavities).

Results and Discussion

In the present study, we consider identical geometry and operation parameters used by Kondo et al.[28] to investigate the shape evolution of electrodeposited copper bumps. Kondo et al.[28–30] studied the electrodeposition of copper bumps using mathematical
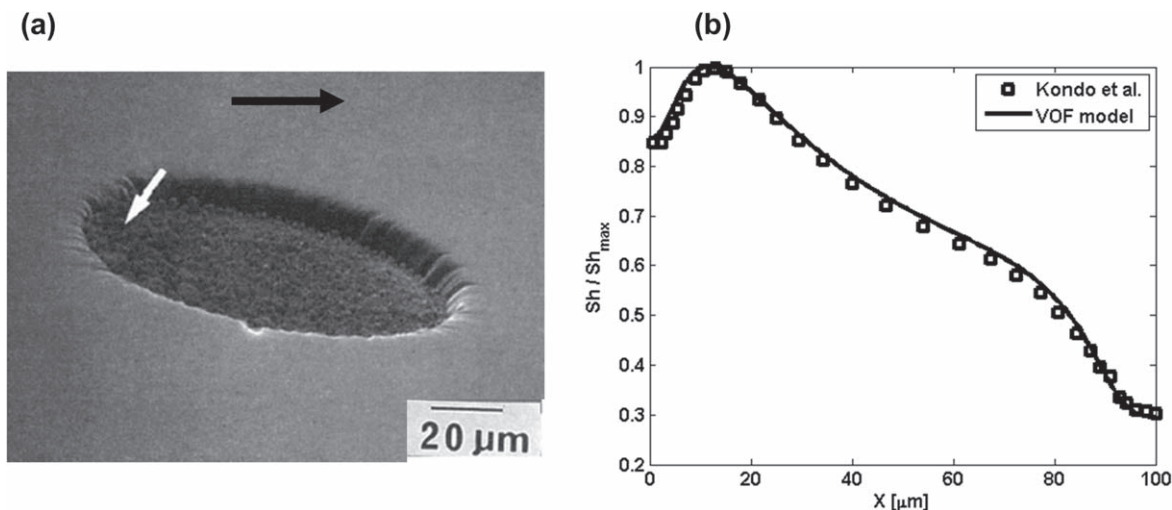
Figure 2. (a) Experimental result reproduced from Ref. 28 where the black arrow shows the direction of flow, and the white arrow indicates the location of maximum height of hump; (b) comparison between our modeling results of the flux (normalized Sherwood number) along the width of cavity and analysis presented by Kondo et al.[28]

Table II. Corresponding boundary conditions of flow, concentration of reactant, and electric current density fields.

Boundary	Conditions
Inlet	$u = \dfrac{u_\infty}{h_{Pe}}(y - h_{Pe}), \dfrac{\partial \varphi}{\partial n} = 0, c = c_\infty$
Outlet	*Pressure-outlet*, $\dfrac{\partial \varphi}{\partial n} = 0, \dfrac{\partial c}{\partial n} = 0$
Insulator	*No-slip*, $\dfrac{\partial \varphi}{\partial n} = 0, \dfrac{\partial c}{\partial n} = 0$
Cathode	*No-slip*, $\varphi = 0, c = 0$
Top	*Free-slip*, $\varphi = V_{app}, c = c_\infty$

Table III. Parameters used in our calculations.

Parameter	
$L_1 [\mu m]$	100
$L_2 [\mu m]$	50
$L_3 [\mu m]$	30
$h_1 [\mu m]$	10
$h_2 [\mu m]$	40
$h_{Pe} [\mu m]$	10
Pe	41.6
$u_\infty [mm \ s^{-1}]$	1.9
$g [m \ s^{-2}]$	9.81
$F [A \ s \ mol^{-1}]$	96485
$V_{app} [V]$	0.45
$\sigma_e [S \ m^{-1}]$	5.1
$\sigma_d [S \ m^{-1}]$	1×10^7
$M [g \ mol^{-1}]$	63.55
$\rho [kg \ m^{-3}]$	1100
$\mu [kg \ m^{-1} \ s^{-1}]$	0.00153
$c_\infty [mol \ m^{-3}]$	600
$D_{Cu^{2+}} [m^2 \ s^{-1}]$	0.45×10^{-9}
$z_{Cu^{2+}}$	$+2$

and experimental tools to explore the effect of flow Peclet number $\left(\text{Pe} = \frac{h_{Pe} \, u_\infty}{D_{Cu^{2+}}}\right)$, and the depth of the cavity on the shape of the deposit.

In the beginning, to verify our VOF based model, we simulated the single cavity for the Peclet number of 41.6. As shown in Fig. 2a, the experimental analysis revealed that the maximum height was located at the upstream side slightly after the circumference of the cavity. The deposit front was observed to be relatively flat at the downstream side. The direction of flow (black arrow) and the location of the maximum height of the hump (white arrow) are shown in Fig. 2a. As illustrated in Fig. 2b, a comparison is made between our modeling results and results obtained by Kondo et al.[28] considering the flux of the reactant ion (normalized Sherwood number). Kondo et al.[28] pointed out that the calculated flux profile (also here using the VOF based model) coincides well with the observed deposit front shape.

Due to the transient character of the electrodeposition process, it is not possible to effectively demonstrate field structures such as flow, the concentration of ion, electric potential, and electric current density. Thus, transient results are shown through animations in supplemental materials, including "Single-cavity.avi" and "Multiple-cavities.avi." Readers are encouraged to make use of these animations. Herein, we illustrate some snapshots at different times of field structures considering the single cavity to explore the interaction between various transport phenomena. Figure 3 illustrates streamlines of flow overlaid on the contour of normalized concentration $\left(\frac{c}{c_\infty}\right)$, magnitude and streamlines of normalized current density

$\left(\frac{j}{j_{max}}\right)$, and normalized equipotential surfaces overlaid on the contour of normalized electric potential $\left(\frac{\varphi}{V_{app}}\right)$. Herein, j_{max} denotes the maximum magnitude of current density, which is placed near the edge of the cavity.

As shown in Fig. 3, geometrical effects lead to a non-uniform distribution of electric current density that, in turn, significantly influences the evolution of the deposited layer. The peak of electric current density is located near the edges of the cavity. The iso-surfaces of electric potential are perpendicular to the streamlines of electric current density. The flow of electrolyte plays a decisive role in the distribution of the reactant over the entire front surface of the deposit. As time advances, increasing the area of the deposit front enhances the uniformity of current density over the deposit front. Indeed, a complex interplay exists between flow, the concentration of reactant, and the evolution of the deposit front. The maximum
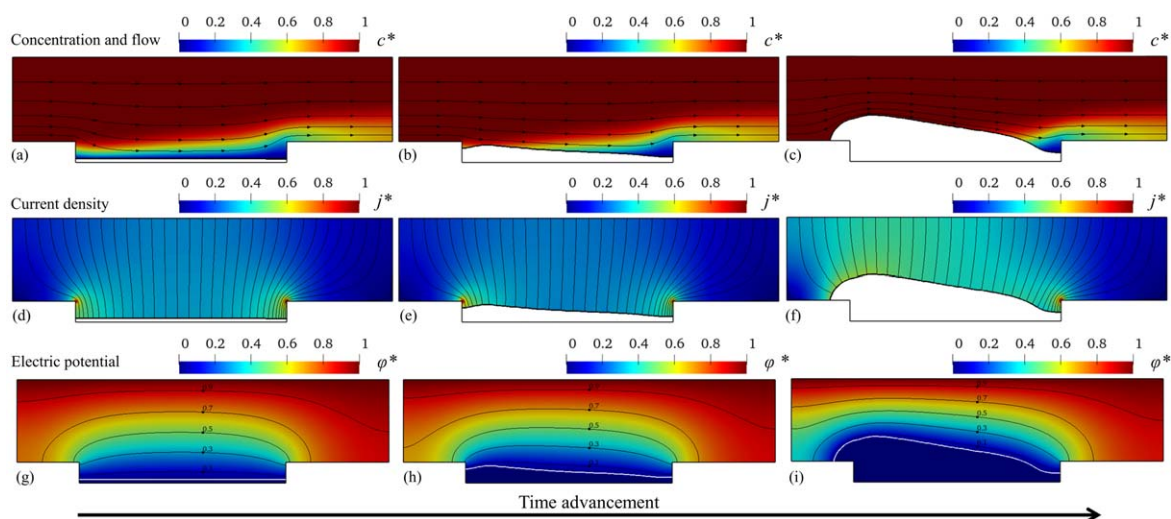
Figure 3. Snapshots at different times of the field structures considering a single cavity are shown. First row including (a)–(c) shows normalized concentration field (c^*) and streamlines of velocity; Second row including (d)–(f) shows current density streamlines and contour of normalized current density (j^*); Third row including (g)–(i) shows contour of normalized potential and normalized equipotential surfaces (ϕ^*). The arrow indicates time advancement.
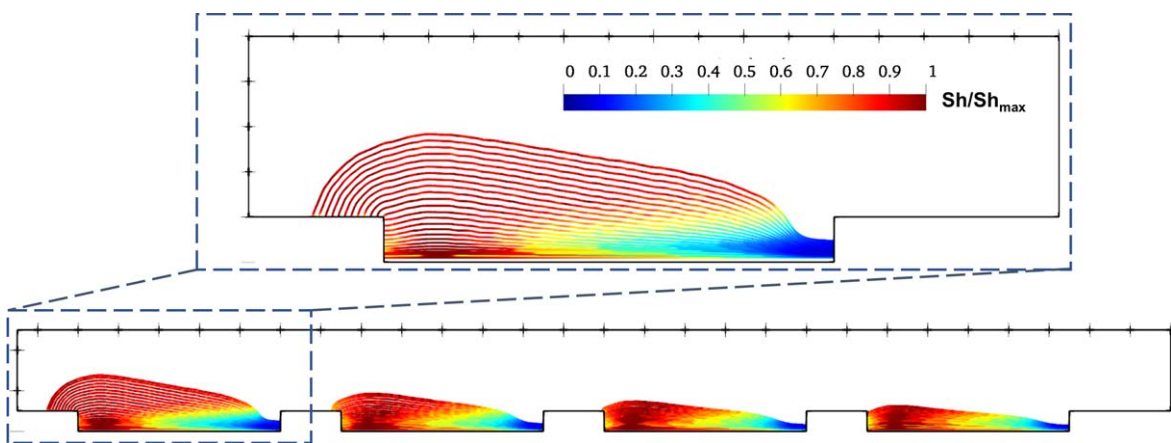
Figure 4. The contour-plot of flux (normalized Sherwood number) captures the evolution of the deposit front. The zoomed area indicates results for the single cavity.

height of the hump remains at the upstream side during the entire electrodeposition process. As time proceeds, the flow pattern and, consequently, the distribution of reactant along the entire surface of the deposit layer are strongly altered. The hump diminishes the transport of fresh reactants to the downstream side of the cavity, where the deposit front lags to grow. As a result, a relatively flat and thin deposit layer forms in the region near the circumference of the downstream side.

Transient field structures considering multiple cavities are shown in the supplemental information "Multiple-cavities.avi." For successive cavities, variation of transport phenomena in the upstream cavities can significantly influence the growth of the deposited layer in the downstream cavities. To further elucidate this phenomenon, the contour-plot of the flux of the reactant ion (normalized Sherwood number) is shown in Fig. 4. The contour-plot is an effective tool to track and to demonstrate the evolution of flux at the deposit front. The growth of the deposit front in the first cavity adjacent to the inlet is unaffected by the transport phenomena in the consecutive cavities. Thus, the zoomed area in Fig. 4 also represents the results of our case study involving a single cavity. As time proceeds, the amplitude of the non-uniformity in the flux at the front of the perpetually growing deposit layer decreases. The height of the hump and the thickness of the deposited layer in each consecutive cavity decreases going from upstream to downstream. In all cavities, the location of the maximum

height of the hump remains invariant at the upstream of each cavity, slightly after the circumference. Also, the deposit exhibits a relatively flat and thin layer at the downstream side of each cavity.

The present study highlights geometrical effects and transport phenomena in the shape evolution of electrodeposited copper bumps. Using simulation results, one can infer the possible cause of the electrolytic flow and the length of the insulators. The proposed VOF based model can aid the industry (e.g. micro-electronics) to get insight into the operation parameters which impact the performance of the process.

Summary

Herein, we put forward a model exploiting the volume of fluid (VOF) method to simulate the transient shape changes of the deposit front, considering the diffusion-limited electrodeposition process. Handling transport phenomena such as flow, the concentration of reactant, electric current density, and electric potential within the electrolyte (fluid) and deposit (solid) are thoroughly discussed. The model is applied to study the shape evolution of electrodeposited copper bumps. Systems involving a single cavity or multiple cavities are investigated. The transient flux of the reactant and, consequently, the transient shape change of the deposit front are computed. The impact of the time-varying thickness of the growth layer on the flux distribution over the entire surface of the deposit front is analyzed.

For the process involving successive cavities, the maximum height of the hump and the thickness of the deposited layer in each consecutive cavity decreases going from upstream to downstream. However, the location of the maximum height of the hump remains invariant at the upstream of each cavity, slightly after the circumference. All transient results are shown through animations in supplemental materials.

ORCID

E. Karimi-Sibaki ⓘ https://orcid.org/0000-0002-2275-6699

References

1. Q.-A. Huang, *Micro Electro Mechanical Systems* (Springer, Singapore) (2020).
2. W. Ruythooren, K. Attenborough, S. Beerten, P. Merken, J. Fransaer, E. Beyne, C. V. Hoof, J. D. Boeck, and J. P. Celis, *J. Micromech. Microeng.*, **10**, 101 (2000).
3. Y. D. Gamburg and G. Zangari, *Theory and Practice of Metal Electrodeposition* (Springer New York, NY, Berlin) (2011).
4. R. Alkire, T. Bergh, and R. L. Sani, *J. Electrochem. Soc.*, **125**, 1981 (1978).
5. N. G. Zamani and F. H. Peters, *Appl. Math. Modell.*, **10**, 262 (1986).
6. D. Wheeler, D. Josell, and T. P. Moffat, *J. Electrochem. Soc.*, **150**, C302 (2003).
7. D. Adalsteinsson and J. A. Sethian, *J. Comput. Phys.*, **122**, 348 (1995).
8. V. R. Subramanian and R. E. White, *J. Electrochem. Soc.*, **149**, C498 (2002).
9. R. Chalupa, Y. Cao, and A. C. West, *J. Appl. Electrochem.*, **32**, 135 (2002).
10. M. Schanz, *Wave Propagation in Viscoelastic and Poroelastic Continua* (Berlin, Springer, Berlin, Heidelberg) (2001).
11. T. O. Drews, S. Krishnan, J. C. Alameda, D. Gannon, R. D. Braatz, and R. C. Alkire, *IBM J. Res. & Dev.*, **49**, 49 (2005).
12. W. Pongsaksawad, A. C. Powell, and D. Dussault, *J. Electrochem. Soc.*, **154**, F122 (2007).
13. D. A. Cogswell, *Phys. Rev. E*, **92**, 011301 (2015).
14. T. Jang, L. Mishra, S. A. Roberts, B. Planden, A. Subramaniam, M. Uppaluri, D. Linder, M. P. Gururajan, J.-G. Zhang, and V. R. Subramanian, *J. Electrochem. Soc.*, **169**, 080516 (2022).
15. M. Hughes, N. Strussevitch, C. Bailey, K. McManus, J. Kaufmann, D. Flynn, and M. P. Y. Desmulliez, *Int. J. Numer. Meth. Fluids*, **64**, 237 (2010).
16. C. Lupo and D. Schlettwein, *J. Electrochem. Soc.*, **166**, D3182 (2019).
17. E. Karimi-Sibaki, A. Kharicha, M. Abdi, M. Wu, A. Ludwig, and J. Bohacek, *J. Electrochem. Soc.*, **166**, D521 (2019).
18. M. Georgiadou, D. Veyret, R. L. Sani, and R. C. Alkire, *J. Electrochem. Soc.*, **148**, C54 (2001).
19. E. J. F. Dickinson, H. Ekström, and E. Fontes, *Electrochemistry Communications*, **40**, 71 (2014).
20. A. Mahapatro and S. Kumar Suggu, *Adv Mater Sci*, **3**, 1 (2018).
21. H. Gu, H. Sun, Y. Xiong, G. Liu, and X. Wang, *J. Appl. Electrochem.*, **48**, 819 (2018).
22. E. Karimi-Sibaki, A. Kharicha, A. Vakhrushev, M. Wu, A. Ludwig, and J. Bohacek, *Electrochem. Commun.*, **112**, 106675 (2020).
23. H. K. Versteeg and W. Malalasekera, *An Introduction to Computational Fluid Dynamics: The Finite Volume Method* (Pearson Education Ltd., Harlow, England; New York) 2nd ed., Vol. 503 (2007).
24. C. W. Hirt and B. D. Nichols, *J. Comput. Phys.*, **39**, 201 (1981).
25. J. S. Newman and N. P. Balsara, *Electrochemical systems* (Wiley, Hoboken, NJ) 4th ed., p. 1 (2019).
26. D. J. Benson, *Appl. Mech. Rev.*, **55**, 151 (2002).
27. ANSYS Fluent 14.5 User's Guide, (2012).
28. K. Kondo, *J. Electrochem. Soc.*, **143**, 1880 (1996).
29. K. Kondo, Y. Suzuki, T. Saito, N. Okamoto, and Y. Koyama, *J. Electrochem. Soc.*, **156**, D548 (2009).
30. K. Kondo, K. Fukui, M. Yokoyama, and K. Shinohara, *J. Electrochem. Soc.*, **144**, 466 (1997).